Calculating the state parameter in crushable sands

Ciantia, Matteo; O'Sullivan, Catherine

Published in:
International Journal of Geomechanics

DOI:
10.1061/(ASCE)GM.1943-5622.0001707

Publication date:
2020

Document Version
Peer reviewed version

Calculating the state parameter in crushable sands

(Matteo Ciantia* & Catherine O'Sullivan)

Abstract

The state parameter (ψ) measures the distance from the current state to the critical state line (CSL) in the compression plane. The existence of a correlation between both the peak angle of shearing resistance (ϕ'_p) and peak dilatancy and ψ is central to many constitutive models used to predict granular soil behaviour. These correlations do not explicitly consider particle crushing. Crushing induced evolution of the particle size distribution influences the CSL position and recent research supports used of a critical state plane (CSP) to account for changes in grading. This contribution evaluates the whether the CSP can be used to calculate ψ and thus enable prediction of the peak angle of ϕ'_p and peak dilatancy where crushing takes place. The data considered were generated from a validated DEM model of Fontainebleau sand that considers particle crushing. It is shown that where ψ is calculated by considering the CSL of the original uncrushed material there can be in a significant error in predicting the material response. Where the CSP is used there is a significant improvement in our ability to predict behaviour whether the CSP is accurately determined using a large number of tests or approximated using crushing yield envelopes. It is shown that the state parameter calculated using the previously available definition can give a false sense of security when assessing liquefaction potential of potentially crushable soils. The contribution also highlights the stress-path dependency of the relationship between ϕ'_p and ψ whichever approach is used to determine ψ.

Keywords

Discrete-element modelling, state parameter; sands; shear strength; stress path; static liquefaction

---

Matteo O. Ciantia*

Lecturer, School of Science and Engineering at Dundee University, School of Civil Engineering,

m.o.ciantia@dundee.ac.uk

Catherine O'Sullivan,

Professor, Dept. Civil and Environmental Engineering, Geotechnics Section, Imperial College

cath.osullivan@imperial.ac.uk

***Corresponding Author**

List of notation

CSP critical state plane

CSL critical state line

CSL^{OC} critical state line of an over consolidated material in which significant crushing has taken place

CSL^{NC} critical state line of a normally consolidated (uncrushed) material

D_{max}^{p} dilatancy at the point where the peak stress ratio is mobilized

e void ratio

e_0 initial void ratio

e_{CS} void ratio on CSL

ICL isotropic compression line

I_G grading state index following Muir Wood and Maeda (2008)

$I_{G,0}$ grading state index based on initial grading

NC normally consolidated

OC over consolidated

p' mean effective stress

$\dot{p}'$ rate of change of mean effective stress with respect to time

p'_{CS} mean effective stress at critical state

q deviator stress

PSD particle size distribution

ϕ'_p peak angle of shearing resistance

ϕ'_{CS} critical state angle of shearing resistance

η stress obliquity, q/p'

ψ state parameter

ψ_0^{CSL} state parameter as the distance to CSL from the initial stress and void ratio

ψ_0^{CSLs} within multiple CSLs, state parameter as the distance to the corresponding CSL from the initial stress and void ratio

ψ_0^{CSP} state parameter as the distance to CSP from initial stress, void ratio and I_G

$\psi_0^{CSP(I_G,cs)}$ state parameter as the distance to CSP from initial stress, void ratio and the measured I_G at CS

$\psi_0^{CSP(I_G,cs,pr)}$ state parameter as the distance to CSP from initial stress, void ratio and the predicted I_G at CS

$\dot{\sigma}'_v$ rate of change of vertical effective stress with respect to time

$\dot{\sigma}'_r$ rate of change of radial effective stress with respect to time

Introduction

A major contribution to the characterization of soil behaviour has been the concept of state parameter. The initial idea of such a measure was first proposed by Wroth and Bassett (1965), then Been and Jefferies (1985) defined their state parameter ψ_0^{CSL} to be the difference in void ratio (e) between the current or initial void ratio e_0 and e_{CS}, .i.e. the value of e on the critical state line (CSL) at the same mean effective stress (p') (Figure 1(a)). An alternative approach to quantify the state of sands is to calculate the distance from the current state to the CSL in terms of a mean stress ratio R_s ($= p'_0/p'_{cs}$) (Coop and Lee, 1993; Jovicic and Coop, 1997), i.e horizontally rather than vertically (in the compression plane). R_s and ψ_0^{CSL} are just different measures of how far the material state is from critical state and, in fact, they can be interconnected analytically. Particle crushing complicates direct application of the state parameter concept as a unique CSL no longer exists (Ghafghazi et al., 2014); there is strong evidence indicating that the *CSL* shifts downwards in *e: p'* space (Bandini and Coop, 2011; Sadrekarimi and Olson, 2014). As detailed in Robertson (2017), due to this downward shift, the material state described by ψ_0^{CSL} is unable to assess material brittleness (Bishop, 1973), while this latter is much better captured by R_s. Also Klotz and Coop (2001) showed that a pressure state parameter performs better for pile driving. Despite the various limitations, it is now well-accepted that use of either ψ_0^{CSL} and R_s can improve our ability to predict sand behaviour (e.g. Azeiteiro et al. (2017), Robertson (2017), Gens (2019)). Nevertheless, the behaviour of soils cannot depend uniquely on the state parameter as other features such as fabric and anisotropy play an important role (Been et al., 1991). The stress levels whereby the evolution of particle crushing becomes significant and starts affecting the soil behaviour vary depending on several aspects including for instance the mineralogic composition of the sand (Leleu and Valdes, 2007) and the initial particle size distribution (Xiao et al., 2018). Whilst for silica sands particle breakage starts to influence the behaviour at pressures of the order of 5-20 MPa, for weaker soils such petroleum coke, pumice and coral carbonate sands such limit ranges from 100 - 500 kPa ((Ciantia et al., 2016; Coop, 1990; McDowell and Bolton, 1998). For example, as discussed in detail by Hyodo et al. (1998) in the Hyogo-ken Nambu, 1995, earthquake, there was widespread liquefaction of land areas reclaimed from the sea using crushable angular soil.

The CSL^{NC} on Figure 1(b) illustrates a normally consolidated material whose *CSL* would translate downwards to the position of CSL^{OC} (*OC* denoting over consolidation) when loaded to a state where significant crushing has occurred. Muir Wood and Maeda (2008) proposed use of a critical state plane (*CSP*) to describe this evolution of the *CSL* position. The CSP is defined in *e*-*p'*-I_G space (Figure 1(c)); I_G, the grading state index, quantifies the amount of crushing that has taken place by considering the particle size distribution (PSD). More recently, and by means of a large number of tests on a ballast-sized material (Tacheng rockfill), Xiao et al., (2016) obtained evidence of *CSL* changes accompanying breakage-induced grading changes and that the critical states are well fitted by a *CSP*. These data were then used to develop a constitutive model for rockfill material (Xiao and Liu, 2017). Ciantia et al., (2019a,b) proposed a simplified method to determine the *CSP* but did not consider how the state parameter should be measured using the CSP. In principle, ψ_0^{CSP} can be

calculated in this three-dimensional space (Figure 1(a)), however the ability of ψ_0^{CSP} to be used as an index to predict mechanical behaviour has not been established. Whichever definition of the state parameter is adopted (i.e. a difference in void ratios or a mean stress ratio) careful consideration must be given to calculating the appropriate distance to the critical state plane. The importance of this is that should the state parameter evolve because of an evolution of I_G during construction or extreme loading of a project (e.g. during pile driving Ciantia et al., (2019c)) then this could have a significant effect on, for example, the liquefaction potential. This contribution fills this knowledge gap by considering a validated discrete element method (DEM) dataset. The use of DEM data enabled detailed analysis of the PSD evolution during shearing; an equivalent laboratory study (see e.g. Lee and Farhoomand (1967)) could only obtain this level of information by repeating the tests, using a new sample each time, and stopping the tests at different levels of deformation to measure the PSDs. In this work we show, for the first time, how the definition of state parameter is ambiguous when the particle size distribution evolves through grain crushing. Further, we present and assess three candidate state parameter definitions capable of handling this change. It is shown that the state parameter calculated using the previously available definition can give a false sense of security when assessing liquefaction potential of potentially crushable soils if the CSL is obtained only using low confinement (uncrushable) tests.

DEM simulations of triaxial shearing of a crushable material

As outlined in Ciantia et al. (2019a) using the PFC3D software (Itasca, 2017) 10,000 spherical particles whose rotation was completely inhibited were assembled in a cubical volume with smooth rigid walls. Crushing was considered to occur if the force at any contact exceeded its limit force, F_{lim}. F_{lim} is determined by considering the contact area, the limit strength of the material and the natural material variability (Ciantia et al., 2015). The model parameters (Ciantia et al., 2019a) were obtained by calibrating the model against experimental data for Fontainebleau sand and this contribution uses DEM results generated in a new analysis of selected numerical data generated in the simulation Series A, E, and F documented in Ciantia et al. (2019a). In series A, E and F crushing is always active (as in real sand), while the simulations on uncrushable samples documented in Ciantia et al. (2019a) (Series B-C-D) are excluded as the focus here is on evaluating the how three possible state parameter definitions perform against real experimental data.

Table 1 summarizes the samples and test simulations considered. For test Series A the initial, normally consolidated (*NC*) states were obtained by isotropic compression; the isotropic compression line (ICL) defined by the initial test states is illustrated on Figure 2(a). For test Series E and F the over consolidated (*OC*) initial states were obtained by isotropic unloading from the *NC* ICL at *p*'=60 MPa and *p*'=100 MPa respectively (Figure 3(a)). In all cases the $I_{G,0}$ value prior to shearing was determined as the area ratio of the current grading to a limit grading following Muir Wood and Maeda, (2008). For the *NC* samples in test Series A $I_{G,0}$ increases with increasing p'_0 for the *OC* tests in Series E and F all tests in each series have the same $I_{G,0}$ (Table 2).

Figure 2(b) illustrates the CSLs for each test series; the differences in stress paths and $I_{G,0}$ are not considered. In line with the observations of Muir Wood and Maeda (2008) the CSL position shifts downwards as grading evolves due to crushing, however each CSL data point has a unique I_G value (Table 1). Figure 2(c) illustrates that the critical state behaviour can be effectively described using a CSP. The CSP defined in Figure 2(c) also gives a good match to the experimental data for Fontainebleau sand (Altuhafi et al., 2018; Luong and Tuati, 1983), confirming the applicability of results to real sand. Figure 2(d) also reports experimentally obtained critical state data for Dogs Bay sand (Bandini and Coop, 2011; Coop and Lee, 1993) reinterpreted using the CSP concept (see Ciantia et al. (2019a) for the CSP fitting parameters of Dog's Bay sand).

Figure 3(a) illustrates the three stress paths followed in q -p' space: (i) conventional trained triaxial compression tests with constant radial stress ($\dot{\sigma}_r'$=0, $\dot{\sigma}_v'$>0, $\dot{p}'$>0) (ii) constant p' tests ($\dot{p}'$=0) and (iii) non-standard drained triaxial compression tests with constant vertical stress ($\dot{\sigma}_v'$=0 , $\dot{\sigma}_r'$<0, $\dot{p}'$<0). Figure 3(b) illustrates the stress-path dependency of the observed responses considering the *NC* sample from test Series A with p'_0 = 6 MPa. The critical state angle of shearing resistance (ϕ'_{CS}), the peak angle of shearing resistance (ϕ'_p) and e_{CS} are clearly stress-path dependent: ϕ'_{CS} , ϕ'_p and e_{CS} are higher for the tests with $\dot{p}'$<0 than for the case with $\dot{p}'$>0. This stress-path dependency is considered further below.

Figure 4(a) shows that both ϕ'_{cs} and ϕ'_p reduce as the mean effective stress at critical state (p'_{cs}) increases; the difference $\phi'_p - \phi'_{cs}$ generally reduces with increasing p'_{cs} (Figure 4(b)). Both Figure 4(a) and (b) indicate a grading dependency; the data for Series E and F where there has been crushing lie below those for Series A and the data for Series A approach the data for Series E and F at larger p'_{cs} values when the I_G values for the tests in Series A approach the I_G values for test Series E and F (Figure 2(c)).

Correlations between the state parameter, mechanical behaviour and liquefaction potential

Figures 5(a) and (b) consider the relationship between $\psi_0^{CSL_A}$ and the observed ϕ'_p and $\phi'_p - \phi'_{cs}$ values respectively; $\psi_0^{CSL_A}$ is calculated using the critical state line obtained for the NC samples (Figure 1(a), CSL_A on Figure 2(b)). For the DEM data the mode of shearing and series ID for each test are identified. Figure 5 includes the experimental data given in Jefferies and Been (2006), the experimental data from Azeiteiro et al. (2017) and reinterpreted experimental results from Luong and Tuati (1983). Full details of the stress paths followed in the experiments considered by Jefferies and Been (2006) are not available. Azeiteiro et al. (2017) considered tests with (i) $\dot{\sigma}_r'$=0, $\dot{\sigma}_v'$>0, $\dot{p}'$>0 and (ii) $\dot{\sigma}_v'$=0, $\dot{\sigma}_r'$<0, $\dot{p}'$<0 on Hostun sand and their data are differentiated by test type. Luong and Tuati, (1983) tests were standard triaxial compression tests on Fontainebleau NC samples and were the ones used to calibrate the DEM model. For test Series A use of $\psi_0^{CSL_A}$ captures the observation by Jefferies and Been (2006) that ϕ'_p and $\phi'_p - \phi'_{cs}$ tend to decrease with increasing ψ and the data lie within

the scatter of the experimental data. For Series E the relationship between ϕ_p' and $\psi_0^{CSL_A}$ plot at the lower limit of the experimental data, and the data for Series F clearly lie below the experimental values. For both Series E and F, use of $\psi_0^{CSL_A}$ fails to capture the expected variation in $\phi_p' - \phi_{cs}'$.

Figures 5(c) and (d) are plots of ϕ_p' against $\psi_0^{CSL_s}$ and $\phi_p' - \phi_{CS}'$ against $\psi_0^{CSL_s}$ respectively, where $\psi_0^{CSL_s}$ is calculated using the CSL obtained the relevant data series, $\psi_0^{CSL_s}$ (Figure 1(b)). It is clear that there is a more consistent relationship between ϕ_p' and $\psi_0^{CSL_s}$ and between $\phi_p' - \phi_{cs}'$ and $\psi_0^{CSL_s}$ in comparison with the trends observed on Figures 5 (a) and (b) where $\psi_0^{CSL_A}$ is considered. The value of $\psi_0^{CSL_A}$ is <0 for test Series F and for most of the tests in Series E and so we would expect these materials to be dilatant with $\phi_p' - \phi_{cs}'$> 0; this is clearly not the case (Figure 5(b)). However when $\psi_0^{CSL_s}$ is used the data points shift to the right and the relationship between $\phi_p' - \phi_{cs}' \approx 0$ and ψ_0 conforms to our expectation of soil behaviour.

Figures 5(e) and (f) explore the relationship between ϕ_p' and ψ_0^{CSP}, where ψ_0^{CSP} is determined by considering the distance to the CSP as illustrated on Figure 1(c). Comparing Figures 5(a) and 5(e) the range of ψ_0^{CSP} values is smaller than the range of $\psi_0^{CSL_A}$ values, with Series E and F having only a very small variation in ψ_0^{CSP} values for the tests considered here. When ϕ_p' is plotted against ψ_0^{CSP} the simulation data do not completely lie within the limits of the experimental data (Figure 5(e)). The data on Figure 5(f) indicate that there is a more consistent relationship between $\phi_p' - \phi_{CS}'$ and ψ_0^{CSP} than there is between $\phi_p' - \phi_{CS}'$ and $\psi_0^{CSL_A}$ (Figure 5(b)) or between $\phi_p' - \phi_{CS}'$ and $\psi_0^{CSL_s}$ (Figure 5(d)).

The stress-path dependency of the material behaviour is evident in Figures 5(a), (c) and (e); the maximum ϕ_p' values are observed for the case with $\dot{\sigma}_v'$=0, while the minimum ϕ_p' occurs where $\dot{\sigma}_r'$=0, and the ϕ_p' values for the $\dot{p}'$=0) are intermediate. This dependency is in agreement with the experimental data of Azeiteiro et al., (2017). While the sensitivity to mode of shearing is less apparent where the $\phi_p' - \phi_{CS}'$ data are considered, in this case the Series A data indicate a higher $\phi_p' - \phi_{cs}'$ value for triaxial extension $\dot{\sigma}_v'$=0 than for triaxial compression $\dot{\sigma}_r'$=0. Referring to Figures 5(b), (d) and (f), as expected, and in agreement with the data from Azeiteiro et al., (2017) the sensitivity of the $\phi_p' - \phi_{cs}'$ data to mode of shearing reduces as ψ_0 increases, for all definitions of ψ_0 considered.

Figure 6 considers the dilatancy at the point where the peak stress ratio is mobilized (D_{max}^p) as a function of ψ_0 considering $\psi_0^{CSL_A}$ (Figure 6(a)), $\psi_0^{CSL_s}$ (Figure 6(b)), and ψ_0^{CSP} (Figure 6(c)), reinterpreted experimental results from Luong and Tuati, (1983) and experimental data from Jefferies and Been, (2006) are included for reference. As before the $\psi_0^{CSL_A}$ values give a misleading impression of soil behaviour for the Series F data and much of the Series E data; suggesting a dilatant response when the sample is contractive (Figure 6(a)). These

data indicate that use of the conventional definition of ψ_0 may not identify the risk of liquefaction in the case where a material is subject to a stress path that induces significant crushing. Referring to Figure 6(b), the relationship between D_{max}^{p} and $\psi_0^{CSL_s}$ is in agreement with our understanding of soil behaviour and the data lie within the bounds of Jefferies and Been's experimental data. Where ψ_0^{CSP} is used there is more scatter amonts the data points and the data extend beyond the lower limit of the experimental values (Figure 6(c)).

The scatter evident in Figure 6(c) prompted consideration about how to calculate ψ_0^{CSP}, these values were calculated using $I_{G,0}$ in line with the use of e_0 . Both I_G and e evolve during shearing but I_G can either increase and evolve towards a maximum value of 1 or remain constant, an alternative definition of the state parameter which makes use of this advantageous feature, $\psi_0^{CSP(I_{G,cs})}$ is proposed; as illustrated in Figure 1(d), $\psi_0^{CSP(I_{G,cs})}$ is calculated considering e_0 , p'_0 and $I_{G,cs}$. Referring to Figures 7(a) and (c) the relationships between ϕ'_p and $\psi_0^{CSP(I_{G,cs})}$ and the relationship between $\phi'_p - \phi'_{CS}$ and $\psi_0^{CSP(I_{G,cs})}$ better confirm with the existing experimental data and our expectations than the data generated using ψ_0^{CSP} (Figures 5(e) and (f)). The scatter observed in the dilatancy data is no longer evident (compare Figures 6(c) and 7(e)).

Use of $I_{G,cs}$ requires knowledge of the PSD at the critical state for every initial state considered. Consequently, practical application of this approach requires a reliable means to predict $I_{G,cs}$. This can be done by fitting the DEM iso-I_G yield envelopes obtained by Ciantia et al, (2019a) with the theoretical yield surfaces proposed in the Kikumoto et al. (2010) model. In the *q*-*p'* plane iso I_G are described as

$$q = mp'\left(2\left(\frac{p_c(I_G)}{p'}-1\right)\right)^{\frac{1}{3}} \tag{1}$$

where m=0.8 is a fitted model parameter and p_c acts as a preconsolidation pressure to which corresponds a unique value of I_G. p_c was obtained fitting the DEM I_G - p' isotropic compression curve by Ciantia et al, (2019a) with the expression proposed by Kikumoto et al. (2010), to account for our initial I_G:

$$I_G = \left\{1-\exp\left[-\left(\frac{p_c - p_{c0}}{p_r}\right)^k\right]\right\}(1-I_{G0}) + I_{G0} \tag{2}$$

with k=2, p_r= 204 MPa, p_{c0}=-26 MPa valid for $p_{c0} > 0$. For a given p_c the values of q and p' that satisfy eq. (1) will then be associated with the I_G obtained with eq. (2) to reconstruct the theoretical iso-I_G maps (Figures 8(a) and (b)). Using this theoretical contour map and given the CSL in the q- p' plane it is possible to predict $I_{G,cs}$ (Figure 8(c)) given the initial state and the stress path. As clearly shown in Figures 8(a) and (b), if the CS points of the overconsolidated samples (series E and F in this case) lie within the I_G yield envelope (dictated by the preconsolidation pressure), the preconsolidation (maximum previous) pressure I_G should be used. If the CS points are outside of the I_G yield envelope, $p_c(I_G)$ evolves and hence the I_G of the corresponding contour should be used. Comparing Figures 7(a) and (b), Figures 7(c) and (d) and Figures 7(e) and (f), it is clear that use of the

predicted $I_{G,cs}$ values to determine $\psi_0^{CSP(I_{G,cs,pr})}$ give correlations very similar to those obtained using $\psi_0^{CSP(I_{G,cs})}$.

To assess the onset of static liquefaction for the initial states considered 24 ancillary DEM undrained (constant volume) compression tests were also run. Half of these are run considering the material to be uncrushable, while crushing was allowed in the remaining simulations. In this way, by comparing the uncrushable and crushable responses, the effect of crushing on the liquefaction potential is better highlighted. In Figure 9(a) the stress paths in the compression plane are presented. In this case only the crushable results are represented. In addition to the initial and final states, and the three CSLs (CSL_A, CSL_E and CSL_F) the figure also reports CSL_{A*} which represents the CSL of the equivalent uncrushable material. CSL_{A*} was obtained by shearing equivalent uncrushable samples (refer to Ciantia et al 2019 for more details). Figure 9 (b-d), illustrates the stress paths in the *q*-*p*' plane; to highlight the effect of breakage, the stress paths of the uncrushable tests are also reported in light grey. Referring to Figure 9(b-d), it can be observed that for test series A, E and F the stress paths initially indicate a decrease in *p*', there is a subsequent stress reversal and *p*' starts to increase until a critical state is attained at the corresponding CSL (CSL_A, CSL_E and CSL_F). The reversal in *p*' does not occur for the tests with 30 MPa confinement in test Series A and E. For these two cases *p*' continues to decrease and the material experiences a softening behaviour characterised by a decrease of deviatoric stress. Note that these two are the only tests for which the initial state lies above CSL_A (the CSL of the normally consolidated samples). On the other hand, the initial state of the 30 MPa confined test Series F lies above CSL_F (but below CSL_A) and does experience the *p*' reversal (no liquefaction). The results clearly show that particle breakage has a big influence on static liquefaction as in some cases the same DEM sample tends to liquefy if crushing is active but doesn't if crushing is inhibited during the undrained shearing. Stress levels of this order of magnitude occur under the tip of piles jacked in sand where particle crushing was found to play an important role in the overall mechanical response (Ciantia et al., 2019c). In the presence of water, particle crushing and dynamic loading associated with pile driving my cause the soil to liquefy. Considering that only the 30 MPa confined test Series A and E clearly show a tendency to liquefy, following Been and Jefferies, (1985), static liquefaction is therefore assessed using the 4 different state parameter definitions reported in Figure 1 and the results of this analysis are summarised in Table 2. Interestingly the Been and Jefferies definition clearly predicts liquefaction potential for all the initial states if the reference CSL is obtained using high pressure triaxial tests of normally consolidated samples (CSL_A). However Been and Jefferies' definition gives a false sense of security when assessing liquefaction if the CSL is obtained only using low confinement (uncrushable) tests ($\psi_0^{CSL_A*}$), indicating the necessity for high pressure triaxial testing if crushing is expected. Use of the CSP with a fixed grading (ψ_0^{CSP}) fails to correctly predict liquefaction because the vertical distance between the initial state and the CSP (constant I_G) does not capture the effect of crushing on volumetric response of the DEM sample. However, $\psi_0^{CSP(I_{G,cs,pr})}$ is also successful, indicating that this approach shows promise as a

predictor of liquefaction potential based on low pressure triaxial and any type of high-pressure laboratory test (e.g. oedometer), rather than specifically high pressure triaxial.

Conclusions

This contribution has re-analysed data from triaxial test simulations carried out using a well-verified DEM model of Fontainebleau sand that can capture particle crushing. Recognising that the critical state locus is better described by a plane in e-p'-I_G space, rather than using a critical state line, the following observations have been made:

1. In presence of crushing, the use of a unique CSL to calculate the initial state parameter ψ_0 , may erroneously predict a dilative response for states that will contract upon shearing, consequently liquefaction susceptibility may be not identified. The use of a CSP to calculate ψ_0 overcomes this limitation.
2. If the initial state parameter ($\psi_0^{CSP(I_{G,cs})}$) is calculated using the CSP and the considering the samples grading at the critical state ($I_{G,cs}$; Fig 1(d)), the correlations between $\psi_0^{CSP(I_{G,cs})}$ and ϕ_p' , $\phi_p' - \phi_{cs}'$ and D_{max}^p are inline with the experimental data from the literature and conventional understanding of state-dependency of soil behaviour.
3. Use of $\psi_0^{CSP(I_{G,cs})}$requires knowledge of $I_{G,cs}$; $I_{G,cs}$ can be predicted using the calibrated grading yield surfaces and preconsolidation pressure expression proposed by Kikumoto et al. (2010).
4. The simulation data presented here indicates that the relationship between ψ_0 and ϕ_p' / $\phi_p' - \phi_{cs}'$ depends on the stress path considered, in agreement with the experimental data from Azeiteiro et al. (2017).
5. Overconsolidated samples, in which significant crushing has occurred, have a smaller range of $\phi_p' - \phi_{CS}'$ and D_{max}^p values in comparison with normally consolidated samples considered over equivalent stress ranges.
6. For more crushable soils such as pumice and coral carbonate sands (where particle crushing appears at much lower pressures) all the above considerations are expected to apply at much lower stresses and further investigation is warranted.

Data Availability Statement

Some or all data, models, or code that support the findings of this study are available from the corresponding author upon reasonable request.

Acknowledgements

Part of this research was supported by the first Author's Junior Research Fellowship at Imperial College London.

References

Altuhafi, F.N., Jardine, R.J., Georgiannou, V.N., Moinet, W.W., Ciantia, M.O., Arroyo, M., Gens, A., 2018. Effects of particle breakage and stress reversal on the behaviour of sand around displacement piles. Géotechnique 1–2.

Azeiteiro, R.J.N., Coelho, P.A.L.F., Taborda, D.M.G., Grazina, J.C.D., 2017. Critical State – Based Interpretation of the Monotonic Behavior of Hostun Sand. J. Geotech. Geoenvironmental Eng. 143, 1–14.

Bandini, V., Coop, M.R., 2011. The influence of particle breakage on the location of the critical state line of sands. Soils Found. 51, 591–600.

Been, K., Jefferies, M.G., 1985. A state parameter for sands. Géotechnique 35, 99–112.

Been, K., Jefferies, M.G., Hachey, J., 1991. The critical state of sands. Géotechnique 41, 365–381.

Bishop, A.W., 1973. The stability of tips and spoil heaps. Q. J. Eng. Geol. Hydrogeol. 6, 335–376.

Ciantia, M.O., Arroyo, M., Butlanska, J., Gens, A., 2016. DEM modelling of cone penetration tests in a double-porosity crushable granular material. Comput. Geotech. 73, 109–127.

Ciantia, M.O., Arroyo, M., Calvetti, F., Gens, A., 2015. An approach to enhance efficiency of DEM modelling of soils with crushable grains. Géotechnique 65, 91–110.

Ciantia, M.O., Arroyo, M., O'Sullivan, C., Gens, A., Liu, T., 2019a. Grading evolution and critical state in a discrete numerical model of Fontainebleau sand. Géotechnique 1–15.

Ciantia, M.O., O'Sullivan, C., Arroyo, M., Gens, A., 2019b. Breakage and critical state via DEM. In: Proceedings of the XVII ECSMGE-2019 Geotechnical Engineering Foundation of the Future.

Ciantia, M.O., O'Sullivan, C., Jardine, R.J., 2019c. Pile penetration in crushable soils: Insights from micromechanical modelling. In: Proceedings of the XVII ECSMGE-2019. Reykjavík, pp. 298–317.

Coop, M.R., 1990. The mechanics of uncemented carbonate sands. Géotechnique 40, 607–626.

Coop, M.R., Lee, I.K., 1993. The behaviour of granular soils at elevated stresses. In: Houlsby, G.T., Wroth, P., Schofield, A.N. (Eds.), Predictive Soil Mechanics. Thomas Telford Ltd, pp. 186–198.

Gens, A., 2019. Hydraulic fills with special focus on liquefaction Remblais hydrauliques en dédiant une attention particulière à la liquéfaction. In: The XVII ECSMGE-2019 Geotechnical Engineering Foundation of the Future. Reykjavík, pp. 1–31.

Ghafghazi, M., Shuttle, D.A., DeJong, J.T., 2014. Particle breakage and the critical state of sand. Soils Found. 54, 451–461.

Hyodo, M., Hyde, A.F.L., Aramaki, N., 1998. Liquefaction of crushable soils. Géotechnique 48, 527–543.

Itasca, 2017. PFC-Particle Flow Code - Version 5.0.

Jefferies, M., Been, K., 2006. Soil Liquefaction: A Critical State Approach. Taylor and Francis.

Jovicic, V., Coop, M.R., 1997. Stiffness of coarse-grained soils at small strains. Géotechnique 47, 545–561.

Kikumoto, M., Wood, D.M., Russell, A., 2010. Particle Crushing and Deformation Behaviour. Soils Found. 50, 547–563.

Klotz, E.U., Coop, M.R., 2001. An investigation of the effect of soil state on the capacity of driven piles in sands. Géotechnique 51, 733–751.

Lee, K.L., Farhoomand, I., 1967. Compressibility And Crushing Of Granular Soil In Anisotropic Triaxial Compression. Can. Geotech. J. 4, 68–86.

Leleu, S.L., Valdes, J.R., 2007. Experimental study of the influence of mineral composition on sand crushing. Géotechnique 57, 313–317.

Luong, M.P., Tuati, A., 1983. Sols grenus sous fortes contraintes. Rev Fr Geotech.

McDowell, G.R., Bolton, M.D., 1998. On the micromechanics of crushable aggregates. Géotechnique 48, 667–679.

Muir Wood, D., Maeda, K., 2008. Changing grading of soil: effect on critical states. Acta Geotech. 3, 3–14.

Robertson, P.K., 2017. Evaluation of Flow Liquefaction: influence of high stresses. In: Proceedings of the 3rd International Conference on Performance Based Design (PBD-III). Vancouver, pp. 1–8.

Sadrekarimi, A., Olson, S., 2014. Residual State of Sands. J. Geotech. Geoenvironmental Eng. 140, 1–10.

Wroth, C.P., Bassett, R.H., 1965. A Stress–Strain Relationship for the Shearing Behaviour of a Sand. Géotechnique 15, 32–56.

Xiao, Y., Liu, H., 2017. Elastoplastic Constitutive Model for Rockfill Materials Considering Particle Breakage. Int. J. Geomech. 17, 04016041.

Xiao, Y., Liu, H., Ding, X., Chen, Y., Jiang, J., Wengang Zhang, 2016. Influence of Particle Breakage on Critical State Line of Rockfill Material. Int. J. Geomech. 16, 04015031.

Xiao, Y., Meng, M., Daouadji, A., Chen, Q., Wu, Z., Jiang, X., 2018. Effects of particle size on crushing and deformation behaviors of rockfill materials. Geosci. Front.

Tables

Table 1. DEM triaxial compression simulations: initial, peak and critical state conditions

		Initial State				Peak State				Critical State			
Test Series	**Stress Path**	e_0 [-]	p'_0 [MPa]	η_0 [-]	$I_{G,0}$ [-]	e_{peak} [-]	p'_{peak} [MPa]	η_{peak} [-]	$I_{G,peak}$ [-]	e_{cs} [-]	p'_{cs} [MPa]	η_{cs} [-]	$I_{G,cs}$ [-]
A	$\dot{\sigma}'_r$=0	0.632	0.5	0	0.737	0.67	1.0	1.52	0.739	0.747	0.9	1.38	0.740
		0.599	6.0	0	0.740	0.59	10.9	1.34	0.753	0.616	10.6	1.28	0.766
		0.561	16.0	0	0.746	0.47	27.2	1.23	0.800	0.466	26.9	1.21	0.808
		0.519	30.0	0	0.754	0.34	49.0	1.16	0.843	0.334	48.7	1.15	0.845
	$\dot{p}'$ =0	0.632	0.5	0	0.737	0.68	0.5	1.53	0.737	0.754	0.5	1.39	0.737
		0.599	6.0	0	0.740	0.62	6.0	1.41	0.746	0.666	6.0	1.32	0.754
		0.561	16.0	0	0.746	0.56	16.0	1.31	0.776	0.563	16.1	1.27	0.778
		0.519	30.0	0	0.754	0.45	30.0	1.23	0.808	0.446	30.1	1.20	0.810
	$\dot{\sigma}'_v$=0	0.632	0.5	0	0.737	0.69	0.2	1.55	0.737	0.759	0.3	1.40	0.737
		0.599	6.0	0	0.740	0.64	3.0	1.47	0.741	0.710	3.2	1.33	0.745
		0.561	16.0	0	0.746	0.60	8.4	1.40	0.750	0.637	8.6	1.30	0.759
		0.519	30.0	0	0.754	0.56	16.0	1.31	0.776	0.556	16.2	1.27	0.781
E	$\dot{\sigma}'_r$=0	0.613	0.5	0	0.779	0.62	1.0	1.43	0.779	0.637	0.9	1.40	0.779
		0.573	6.0	0	0.779	0.57	10.8	1.33	0.784	0.570	10.7	1.32	0.786
		0.533	16.0	0	0.779	0.46	27.3	1.25	0.806	0.461	27.3	1.24	0.809
		0.494	30.0	0	0.779	0.33	49.1	1.20	0.825	0.333	49.0	1.16	0.845
	$\dot{p}'$ =0	0.613	0.5	0	0.779	0.62	0.5	1.44	0.779	0.642	0.5	1.41	0.779
		0.573	6.0	0	0.779	0.59	6.0	1.36	0.780	0.603	6.0	1.34	0.781
		0.533	16.0	0	0.779	0.53	16.0	1.32	0.788	0.536	16.0	1.31	0.789
		0.494	30.0	0	0.779	0.45	30.0	1.25	0.803	0.445	30.0	1.24	0.810

	$\dot{\sigma}_v'$=0	0.613	0.5	0	0.779	0.62	0.3	1.45	0.779	0.650	0.3	1.42	0.779
		0.573	6.0	0	0.779	0.60	3.1	1.38	0.779	0.621	3.2	1.35	0.780
		0.533	16.0	0	0.779	0.57	8.4	1.35	0.779	0.584	8.5	1.33	0.784
		0.494	30.0	0	0.779	0.54	15.9	1.32	0.784	0.540	16.0	1.30	0.789
F	$\dot{\sigma}_r'$=0	0.537	0.5	0	0.820	0.53	0.9	1.41	0.820	0.533	0.9	1.36	0.820
		0.507	6.0	0	0.820	0.47	10.8	1.32	0.820	0.478	10.7	1.31	0.823
		0.469	16.0	0	0.820	0.40	27.7	1.27	0.827	0.402	27.5	1.25	0.836
		0.430	30.0	0	0.820	0.33	49.2	1.17	0.840	0.309	48.6	1.17	0.856
	$\dot{p}'$ =0	0.537	0.5	0	0.820	0.54	0.5	1.43	0.820	0.539	0.5	1.39	0.820
		0.507	6.0	0	0.820	0.49	6.0	1.34	0.820	0.502	6.0	1.32	0.820
		0.469	16.0	0	0.820	0.45	16.0	1.31	0.820	0.456	16.0	1.28	0.824
		0.430	30.0	0	0.820	0.40	30.0	1.25	0.825	0.394	30.0	1.23	0.833
	$\dot{\sigma}_v'$=0	0.537	0.5	0	0.820	0.54	0.3	1.44	0.820	0.548	0.3	1.39	0.820
		0.507	6.0	0	0.820	0.52	3.1	1.40	0.820	0.522	3.2	1.36	0.820
		0.469	16.0	0	0.820	0.49	8.5	1.34	0.820	0.493	8.5	1.31	0.822
		0.430	30.0	0	0.820	0.45	16.0	1.32	0.820	0.454	16.1	1.29	0.826

Table 2. State parameters and static liquefaction assessment

Test Series	$\psi_0^{CSL_A}$	$\psi_0^{CSL_A*}$	ψ_0^{CSLs}	ψ_0^{CSP}	$\psi_0^{CSP(I_{G,cs,pr})**}$	*Static Liquefaction via DEM*
A	-0.120	-0.136	-0.120	-0.117	-0.122	X
	-0.068	-0.133	-0.068	-0.111	-0.091	X
	-0.004	-0.125	-0.004	-0.095	-0.035	X
	0.068	-0.112	**0.068**	-0.072	**0.041**	**LIQUEFACTION**
E	-0.140	-0.136	-0.031	-0.034	-0.035	X
	-0.095	-0.133	-0.030	-0.041	-0.042	X
	-0.032	-0.125	-0.003	-0.042	-0.042	X
	0.043	-0.112	**0.047**	-0.037	**0.029**	**LIQUEFACTION**
F	-0.216	-0.136	-0.003	-0.011	-0.011	X
	-0.160	-0.133	**0.001**	-0.008	-0.008	X
	-0.096	-0.125	**0.014**	-0.007	-0.006	X
	-0.021	-0.112	**0.040**	-0.002	-0.001	X

*CSL for low confinement (uncrushable DEM tests)

** Used $\dot{p}'$ =0 stress path to predict $I_{G,CS}$

Figures

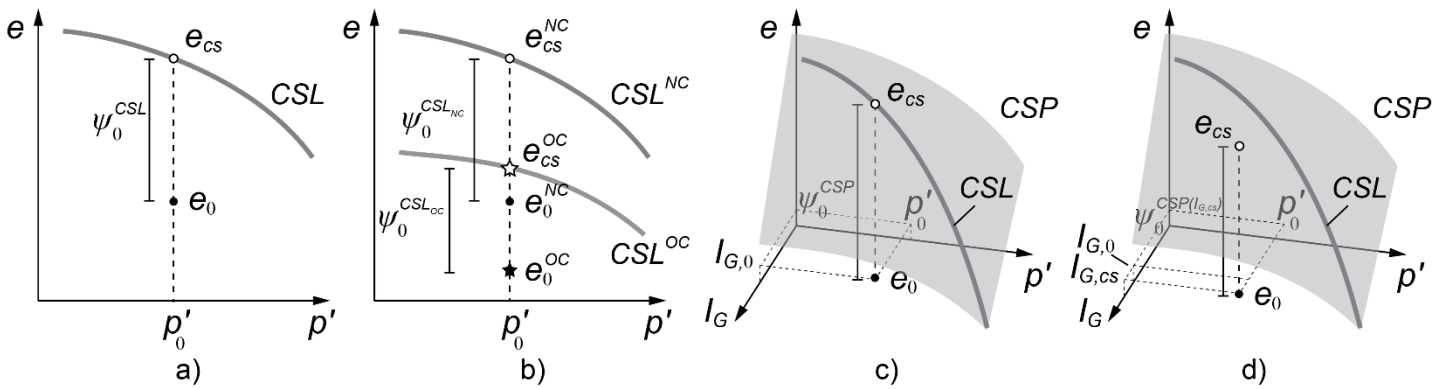

Figure 1. Definitions of state parameter for crushable material: a) Been and Jefferies classic definition ψ=e_0-e_{cs}, b) Been and Jefferies definition applied to crushable materials considering multiple CSLs; c) Been and Jefferies definition applied using the CSP; d) Been and Jefferies definition applied using the CSP and e_0, p'_0 and $I_{G,cs}$ as initial state.

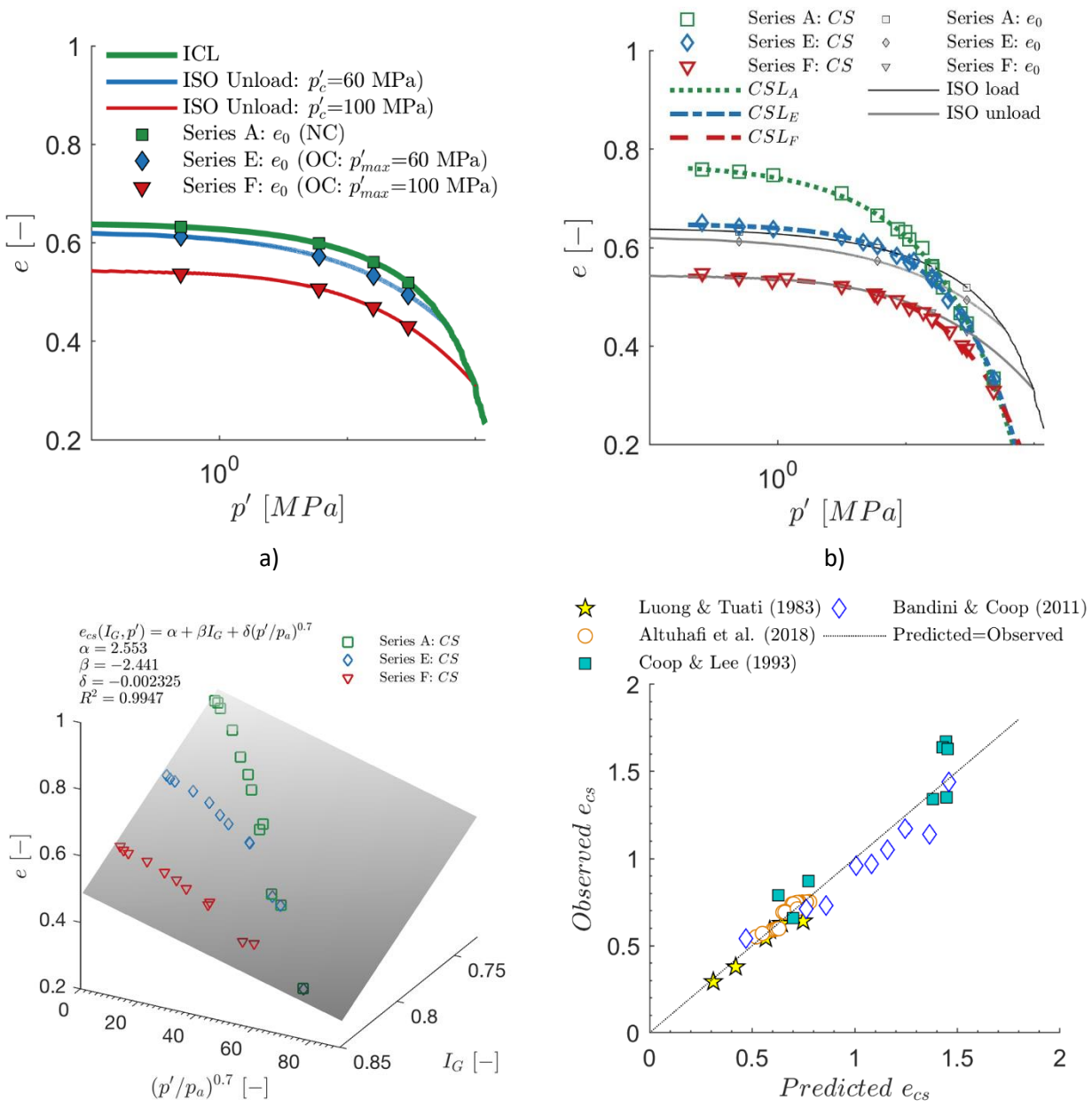

Figure 2. Normally consolidated (NC) and over consolidated (OC) initial states (a) and corresponding critical state (CS) points obtained by Ciantia et al., (2019a) fitted by three critical state lines, CSL_A, CSL_E and CSL_F (b); (c) CS fitted by a CSP function of I_G-e-p′ and (d) comparison of numerically predicted (using the CSP in c) and experimentally obtained critical state data for Fontainebleau sand. Data for Dogs Bay sand reinterpreted using the CSP concept is also reported (see Ciantia et al., 2019a for CSP parameters).

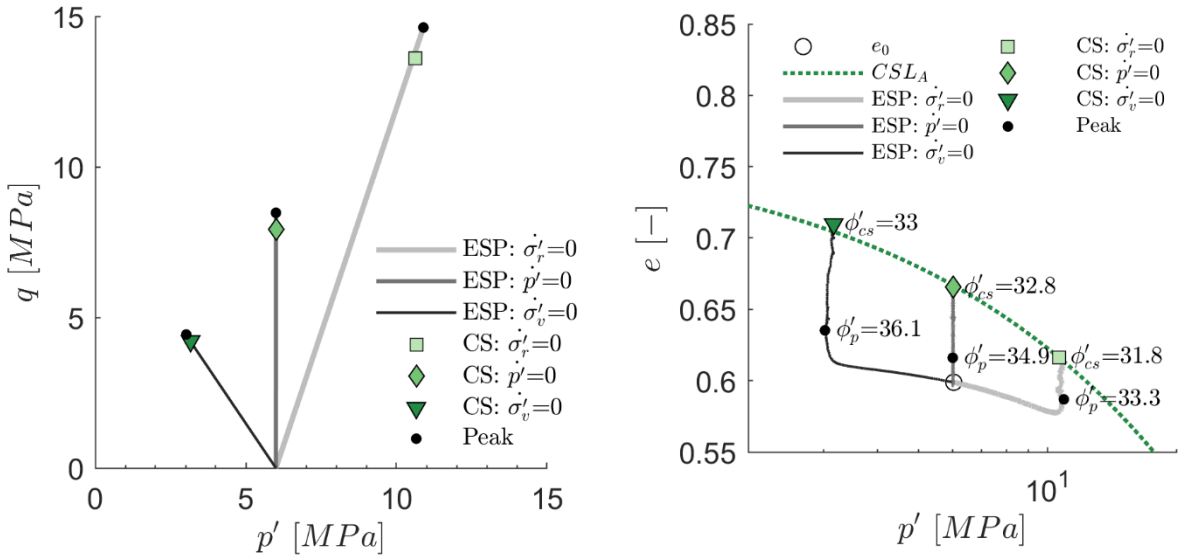

a) b)

Figure 3. Responses observed on three representative tests from simulation series A (crushable material; OCR=1, initial confining pressure=6 MPa): (a) effective stress paths (ESP), peak and critical state envelopes; (b) ESP in the compression plane.

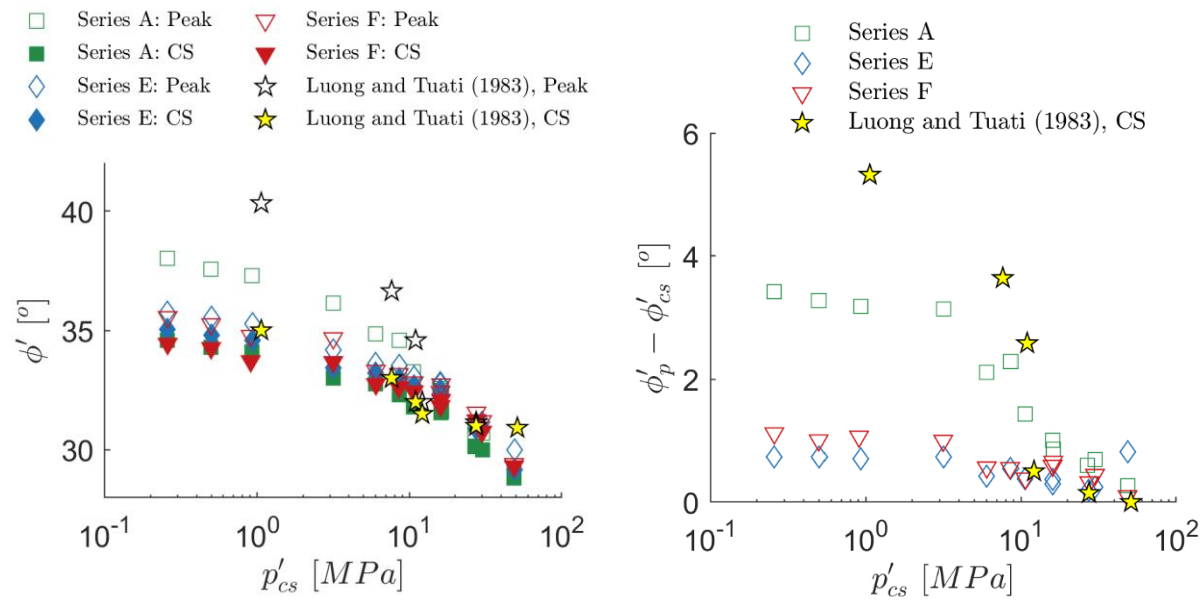

a) b)

Figure 4. Mean effective pressure confinement effect on peak and critical state friction angle on normally consolidated, NC, (Series A) and over consolidated, OC, (Series E,F). Luong and Tuati, (1983) NC experimental data for Fontainebleau sand is also represented.

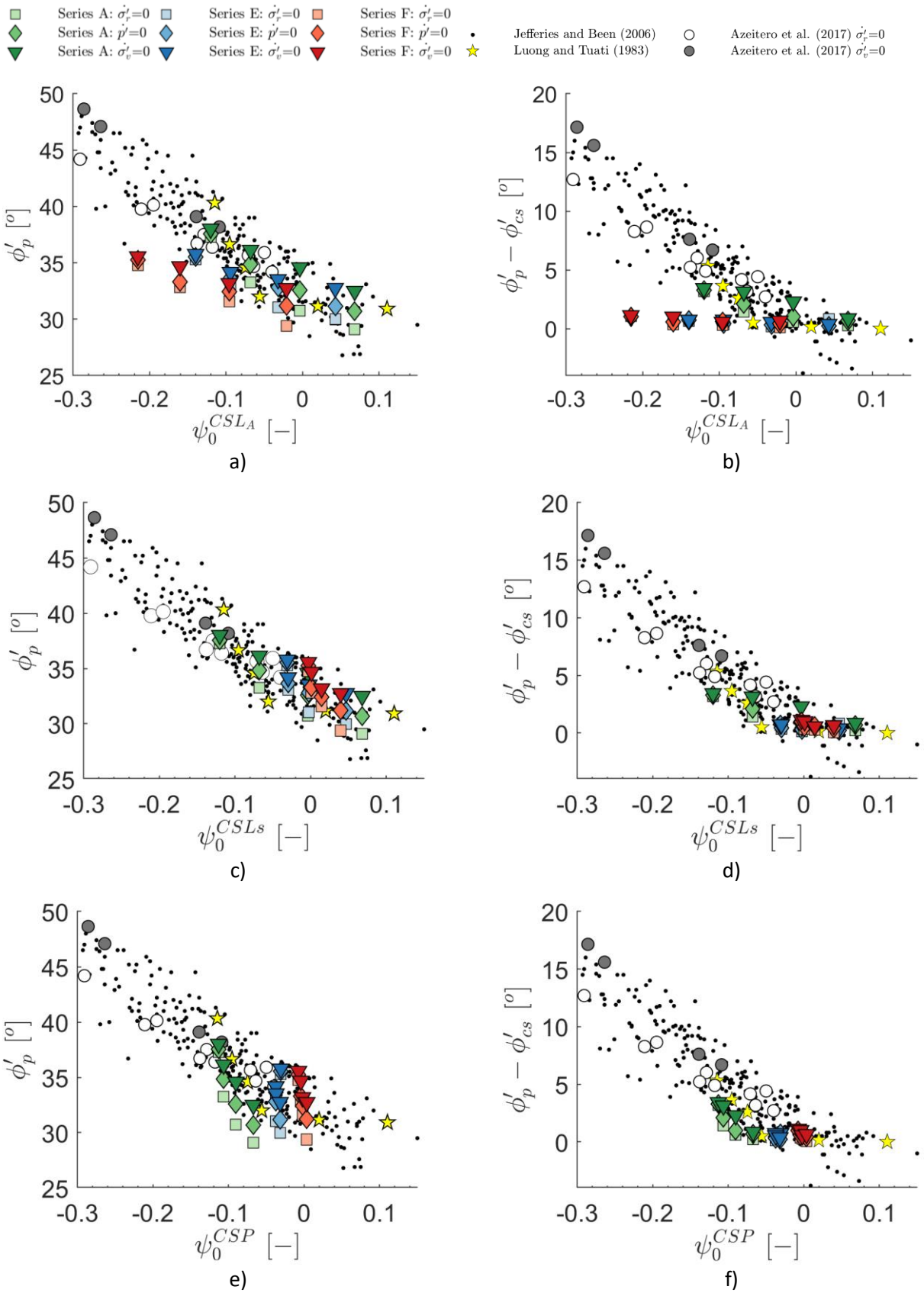

Figure 5. Relationship between the angle of shearing resistance and the initial state parameter defined using: (a,b) a single critical state (CSL_A) obtained using NC samples; (c,d) three critical state lines, CSLs, (CSL_A, CSL_E and CSL_F) and the corresponding initial states; e,f) the critical state plane (CSP). DEM simulation results presented along with the experimental data reported in Jefferies and Been (2006) and re-elaborated data from Azeitero et al. (2017) and Luong and Tuati, (1983).

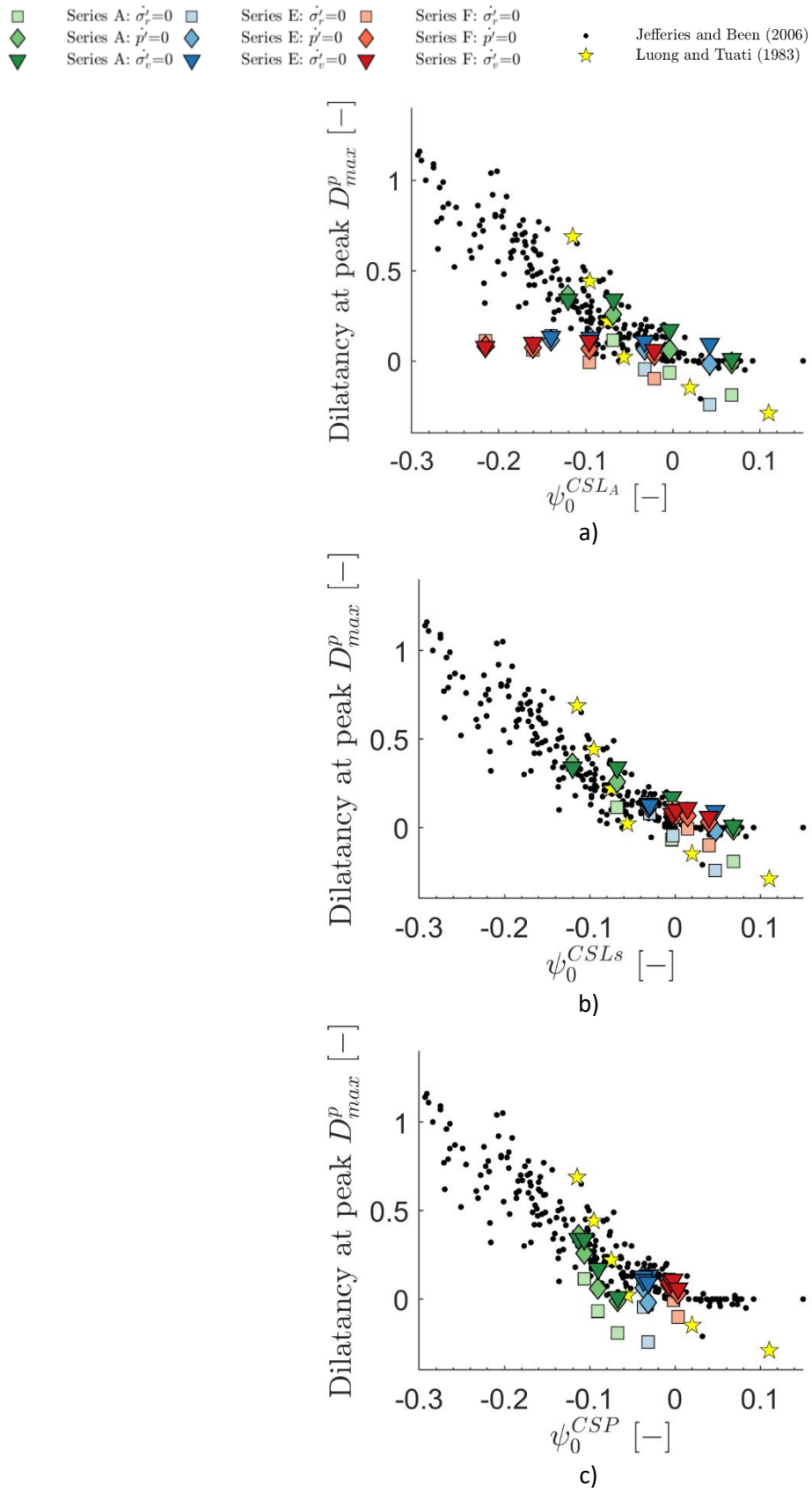

Figure 6. Relationship between the peak dilatancy and the initial state parameter defined using: a) a single critical state (CSL_A) obtained using NC samples; b) three critical state lines (CSL_A, CSL_E and CSL_F) and the corresponding initial states; c) the critical state plane (CSP). DEM simulation results presented along with the experimental data reported in Jefferies and Been (2006).

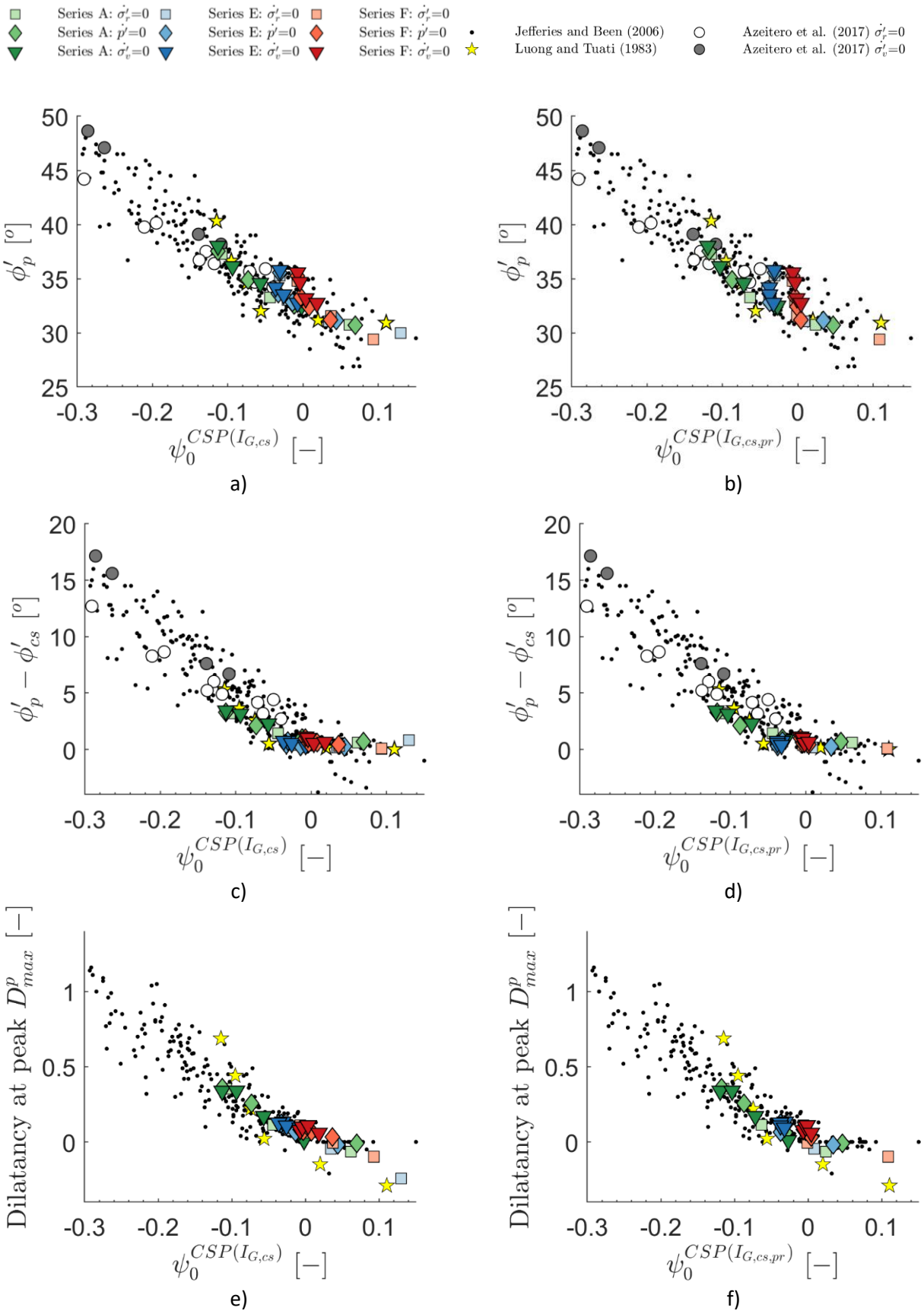

Figure 7. Relationship between the angle of shearing resistance - peak dilatancy and the initial state parameter defined using the critical state plane (CSP) evaluated using the grading index at critical state. This latter can be estimated beforehand using the iso I_G maps obtained by Ciantia et al. 2019a.

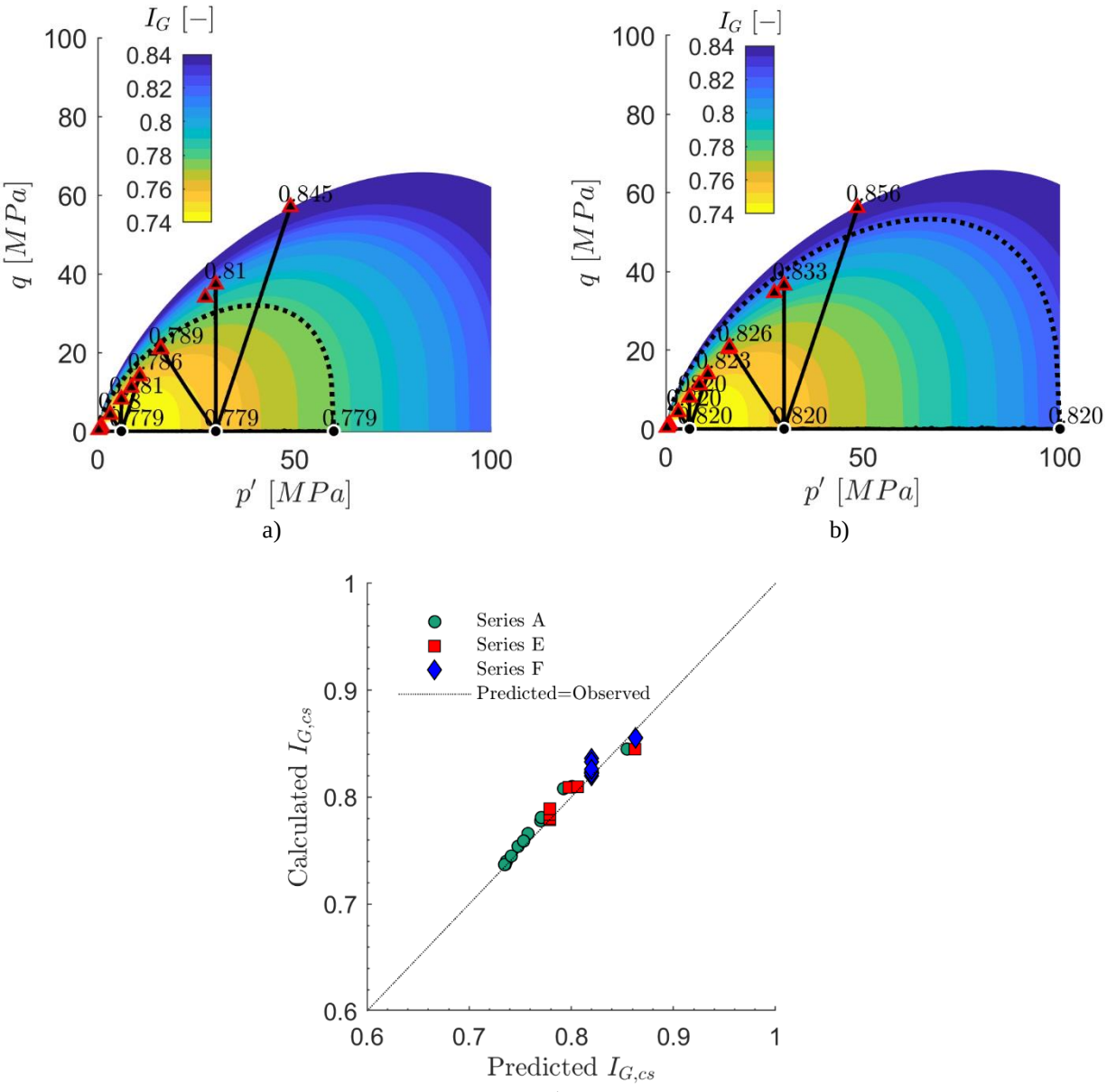

Figure 8. iso-I_G map obtained fitting the Grading yield function by Kikumoto et al. (2010) to DEM data by Ciantia et al., (2019a) for series E (a) and F (b) and corresponding predicted and calculated I_G at critical state. For the latter, the CS points lying within the I_G yield locus are assigned their corresponding over consolidated I_G (i.e 0.779 and 0.820 for series E and F respectively).

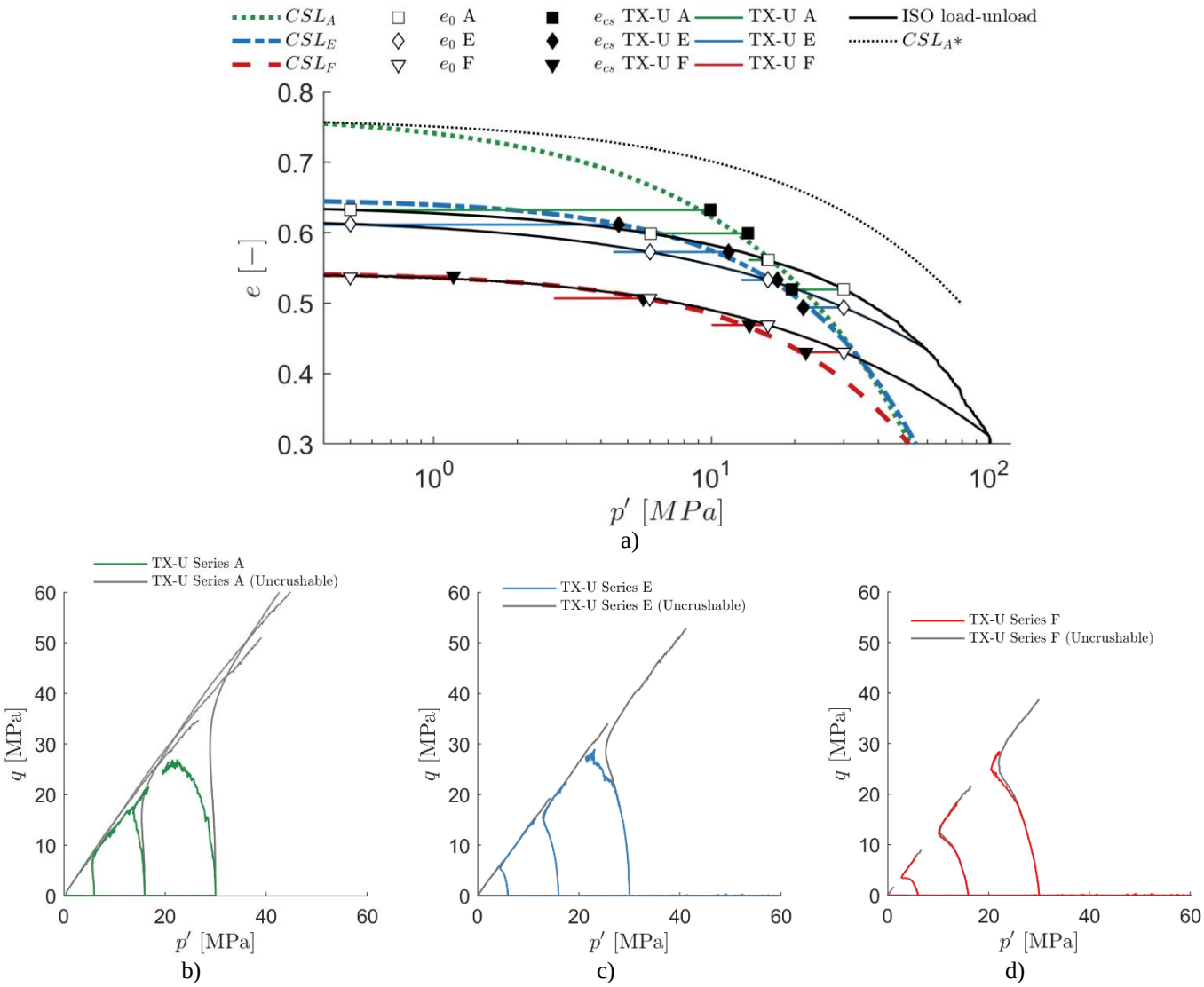

Figure 9. Stress paths of undrained triaxial (constant volume) compression tests represented in the a) compression plane, b-d) the triaxial plane.